



Suppressing the metal-metal interaction by $\text{CoZn}_{0.5}\text{V}_{1.5}\text{O}_4$ derived from two-dimensional metal-organic frameworks for supercapacitors

Fang Yuan¹, Guohua Gao^{1*}, Xiaodi Jiang¹, Wenchao Bi^{2*}, Yixuan Su¹, Jingwen Guo², Zhihao Bao¹, Jun Shen¹ and Guangming Wu^{1*}

ABSTRACT Co_2VO_4 with Co tetrahedrons and octahedrons of transition metal oxides has achieved progress in electrocatalysts and batteries. However, high metal-metal interactions make it challenging to maintain high reactivity as well as increase the conductivity and stability of supercapacitors. In this work, spinel-structured $\text{CoZn}_{0.5}\text{V}_{1.5}\text{O}_4$ with a high specific surface area was synthesized through an ion-exchange process from the metal-organic frameworks of zinc-cobalt. Density functional theory calculations indicate that the replacement of transition metal by Zn can decrease the interaction between the transition metals, leading to a downshift in the π^* -orbitals (V–O) and half-filled a_{1g} orbitals near the Fermi level, thus increasing the conductivity and stability of $\text{CoZn}_{0.5}\text{V}_{1.5}\text{O}_4$. As a supercapacitor electrode, $\text{CoZn}_{0.5}\text{V}_{1.5}\text{O}_4$ exhibits high cycling durability (99.4% capacitance retention after 18,000 cycles) and specific capacitance (1100 mF cm^{-2} at 1 mA cm^{-2}). This work provides the possibility of designing octahedral and tetrahedral sites in transition metal oxides to improve their electrochemical performance.

Keywords: supercapacitors, metal-metal interaction, octahedral, tetrahedral, metal-organic frameworks

INTRODUCTION

To mitigate energy crisis, it is important to develop high-efficiency energy storage devices with high energy density, high power density, and long cycling life [1–3]. Supercapacitors, emerging as energy storage devices, have received increasing attention in electric vehicles, intermittent wind, and solar energy systems owing to their short charge-discharge time, high power density, long cycle life, and high safety [4–8]. The electrode materials of supercapacitors can be divided into carbon materials, conductive polymers, and transition metal oxides according to different charge storage mechanisms [9]. Electric double-layered capacitive carbon materials that store charges with fast ion adsorption and desorption on the electrode surface can achieve high power density and long life; however, their theoretical specific capacitance is low [10,11]. Pseudocapacitive conductive polymers, N-doped carbon materials, and transition metal oxides provide higher theoretical specific capacitance owing to their fast redox reactions at the electrode/electrolyte interface [12–14]. However, conductive polymers usually exhibit

poor durability, which limits their wide range of applications [15]. For N-doped carbon materials, lone-pair electrons of N can enhance the pseudocapacitance storage, but the energy density per unit mass is still limited [16–19]. Transition metal oxides, such as Co and V, which exhibit higher theoretical capacitance owing to their high oxidation state, have been considered as promising electrode materials for supercapacitors. After decades of development, research on both the capacity and stability of transition metal oxides for supercapacitors has achieved great progress [13]; however, the areal energy density remains a challenge for future applications. To increase the number of active sites per unit area, nanostructures with super-high specific area have constantly been chosen, which decrease the stability during charging and discharging cycles [20].

Recently, spinel structures composed of tetrahedrons and octahedrons of transition oxides have attracted significant attention in electrocatalysts and batteries [21–23]. Mu *et al.* [21] designed an ideal electronic configuration of Co_2VO_4 by introducing $\text{Co}(\text{O}_6)$ octahedrons, which exhibits a low-spin state with one e_g electron and outstanding electrocatalytic performance. Liu *et al.* [24] synthesized the disordered rock salt oxide, $\text{Li}_{3+x}\text{V}_2\text{O}_5$, which can be used as a fast charge cathode material for lithium-ion batteries. According to the distribution of the Li/V tetrahedron and octahedron, the optimal transport path of lithium ions in $\text{Li}_{3+x}\text{V}_2\text{O}_5$ will change from a tetrahedron-octahedron-tetrahedron (t-o-t) transition to a direct tetrahedron to tetrahedron (t-t) transition, which causes rapid lithium-ion conduction. However, the low intrinsic conductivity of Co_2VO_4 [21] is caused by the interaction between transition metals, such as Co and V, which causes the d orbital near the Fermi level to split into bonding a_{1g} and anti-bonding combination a_{1g}^* , thus creating a bandgap. Therefore, it is important to replace the octahedron of $\text{Co}(\text{O}_6)$ with a late transition metal, whose outermost electrons are in the deep energy level. For instance, when Zn is introduced to form $\text{Zn}_x\text{Co}_{1-x}\text{O}$, some new electronic states appear in the band gap of density of states (DOS), thereby increasing the carrier density of the material and improving the conductivity [25]. Yang *et al.* [26] found that the layered structure of Zn-doped Ni-metal-organic framework (MOF) can greatly enhance the specific capacitance and stability of supercapacitor electrode materials. Further, it can achieve high capacitances of 1620 F g^{-1} at 0.25 A g^{-1} ; the capacitance loss is only 8% after 3000 cycles. Thus, we hypothesize that if Zn

¹ Shanghai Key Laboratory of Special Artificial Microstructure Materials and Technology, School of Physics Science and Engineering, Tongji University, Shanghai 200092, China

² College of Science, University of Shanghai for Science and Technology, Shanghai 200093, China

* Corresponding authors (emails: gao@tongji.edu.cn (Gao G); bi_wenchao@126.com (Bi W); wugm@tongji.edu.cn (Wu G))

replaces Co on octahedral sites, the conductivity can be improved by weak Zn–V interactions; the stability can be improved by the Zn–O covalent bonds; the reaction sites will be maintained by Co on tetrahedral sites, which will promote the electrochemical activity and stability of Co_2VO_4 .

Moreover, the specific capacitance of supercapacitors is closely related to the specific surface area of the electrode materials [27–29]. MOFs have unique physicochemical properties owing to their specific morphologies and high specific surface areas [29–35]. They reveal many advantages in gas separation, fluorescence sensing, catalysis, electrochemistry, and other fields [36–38]. For example, Bai *et al.* [36] reported Ni/Co bimetallic MOF nanoplates, which exhibited excellent oxygen evolution reaction electrocatalytic activity with a low overpotential of 256 mV at 10 mA cm^{-2} and a small Tafel slope of 81.8 mV dec^{-1} in KOH with long-term electrochemical stability for 3000 cyclic voltammetry (CV) cycles. The recrystallization process of MOFs can maintain their original morphology and introduce doping atoms for functional applications, such as porous carbon [39,40], metal oxides [41,42], and sulfides [43,44]. Guan *et al.* [41] reported hollow and porous NiCo_2O_4 nanostructures fabricated using two-dimensional solid nanowall arrays of Co-MOF through an ion-exchange and etching process with an additional annealing treatment. The as-fabricated NiCo_2O_4 nanowall electrode shows remarkable capacitance (1055.3 F g^{-1} at 2.5 mA cm^{-2}). Young *et al.* [42] converted the bimetallic NiCo-MOF-74 particles into graphitic carbon/ $\text{Ni}_x\text{Co}_{1-x}$ composites and $\text{Ni}_x\text{Co}_{1-x}/\text{Ni}_x\text{Co}_{1-x}\text{O}$ composites, which exhibited high specific capacitances of 715 and 513 F g^{-1} , respectively. Zhang *et al.* [45] utilized porous graphitic carbon, which was co-doped with N and S, to encapsulate Co_9S_8 MOFs ($\text{Co}_9\text{S}_8/\text{NS-C}$) to enhance the stability of the electrode (capacitance retention of 99.8% after 140,000 cycles).

In this study, we propose a simple method to synthesize $\text{CoZn}_{0.5}\text{V}_{1.5}\text{O}_4$ through the ion-exchange and recrystallization of MOFs of zinc-cobalt (ZnCo-MOF) and sodium metavanadate (NaVO_3). As a late transition metal, Zn assumes the place of the Co octahedron, which was identified by Raman and X-ray photoelectron spectroscopy (XPS). According to theoretical calculations, the $\text{Co}(\text{O}_6)\text{-V}$ interaction repels the 3d orbital near the Fermi level and acts as a semiconductor. The doping of Zn can decrease the metal-metal effect and result in exits of the degenerate state at the Fermi level. The synthesized samples of $\text{CoZn}_{0.5}\text{V}_{1.5}\text{O}_4$ exhibit high specific capacitance (1100 mF cm^{-2} at a current density of 1 mA cm^{-2}), enhanced rate capability (81% specific capacitance retention after 10 times increase in the current density), and long cycling durability (99.4% capacitance retention after 18,000 cycles).

EXPERIMENTAL SECTION

Fabrication of ZnCo-MOF

Approximately 1 mmol zinc nitrate hexahydrate ($\text{Zn}(\text{NO}_3)_2 \cdot 6\text{H}_2\text{O}$) and 2 mmol cobalt nitrate hexahydrate ($\text{Co}(\text{NO}_3)_2 \cdot 6\text{H}_2\text{O}$) were dissolved in 50 mL of deionized water and stirred at room temperature for 30 min to form solution A. Thereafter, 16 mmol 2-methylimidazole (2-MIM) was dissolved in another 50 mL of deionized water and stirred for 30 min to obtain solution B. Solution A was added quickly to solution B, and then stirred vigorously for 1 min. Subsequently, a piece of cleaned nickel foam (NF) (2 cm \times 4 cm) was washed with

0.5 mol L^{-1} hydrochloric acid, ethanol, and water in turn and then immersed into the above mixture for ZnCo-MOF precursor growth. After 3 h, the NF turned purple and was removed from the mixture and washed several times with deionized water and ethanol. Thereafter, it was vacuum-dried at 60°C for 8 h.

Synthesis of $\text{CoZn}_{0.5}\text{V}_{1.5}\text{O}_4$

A piece of the as-fabricated NF with ZnCo-MOF was immersed in a solution of 4 mmol L^{-1} NaVO_3 . After 2 h of reaction at room temperature, it was removed, cleaned with deionized water, and then dried in a vacuum oven at 60°C for 8 h. Thereafter, it was heated in a muffle furnace at 250°C for 2 h to obtain the $\text{CoZn}_{0.5}\text{V}_{1.5}\text{O}_4$ sample, which was grown on NF ($\text{CoZn}_{0.5}\text{V}_{1.5}\text{O}_4/\text{NF}$). The mass loading of $\text{CoZn}_{0.5}\text{V}_{1.5}\text{O}_4$ was ~ 2.11 mg cm^{-2} .

Synthesis of Co_2VO_4

Solution A was synthesized using 2 mmol of $\text{Co}(\text{NO}_3)_2 \cdot 6\text{H}_2\text{O}$ dissolved in 50 mL deionized water. The other steps were the same as those used for the fabrication of ZnCo-MOF and $\text{CoZn}_{0.5}\text{V}_{1.5}\text{O}_4$ to acquire Co-MOF and Co_2VO_4 , respectively. Similarly, we obtained a sample of Co_2VO_4 grown on NF ($\text{Co}_2\text{VO}_4/\text{NF}$). The mass loading of Co_2VO_4 was ~ 2.04 mg cm^{-2} .

Material characterization

The morphologies and structures of the samples were characterized by scanning electron microscopy (SEM, S-4800), transmission electron microscopy (TEM, JEOL-2100), and high-resolution TEM (HRTEM, field emission JEOL-2100). The crystalline structure of the material was investigated by X-ray diffraction (XRD, RigataD/max-C diffractometer with a Cu-K α radiation source, $\lambda = 1.5406$ Å) over the 2θ range of 10° to 80°. The elements on the surface were analyzed by XPS (RBD upgraded PHI-5000C ESCA system with Mg-K α radiation, $h\nu = 1253.6$ eV). Raman spectra were obtained on a Raman spectrometer (Jobin-Yvon HR800) from 200 to 1600 cm^{-1} using a 514 nm argon ion laser. Nitrogen adsorption/desorption isotherms and Barrett-Joyner-Halenda (BJH) pore diameter distribution curves were characterized using a Quantchome Autosorb-1 analyzer.

Electrochemical measurements

The electrochemical performances of the as-obtained electrodes were characterized using a three-electrode system in an electrolyte of 2 mol L^{-1} KOH aqueous solution. A platinum foil (1 cm \times 1 cm) and a saturated calomel electrode (SCE) were used as the counter electrode and reference electrode, respectively. $\text{CoZn}_{0.5}\text{V}_{1.5}\text{O}_4$ and Co_2VO_4 were used as working electrodes directly without any binder, metal support, or current collector. The NF with the active material was cut into small pieces of 1 cm \times 1 cm and immersed in the electrolyte for testing. CV, galvanostatic charge/discharge (GCD), and electrochemical impedance spectroscopy (EIS) were performed using an electrochemical workstation (CHI 660E, Shanghai Chenhua Instrument Company, Shanghai, China). The voltage range of CV was 0–0.45 V, and the scanning rate was 5–100 mV s^{-1} . The voltage range of GCD was 0–0.45 V, and the current density was 1–10 mA cm^{-2} . The EIS performance test frequency range was 10^{-2} – 10^5 Hz, and the alternating current amplitude was 5 mV. The specific capacitance (C , mF cm^{-2}), energy density (E , mW h cm^{-2}), and power density (P , mW cm^{-2}) were calculated using the following formulas:

$$C = \frac{I\Delta t}{S\Delta V}, \quad (1)$$

$$E = \frac{1}{7200}C(\Delta V)^2, \quad (2)$$

$$P = 3600\frac{E}{\Delta V}, \quad (3)$$

where I is the constant discharge current (mA), Δt is the discharge time (s), S is the effective area of the active substance of the work electrode (cm^2), and ΔV is the discharge voltage range (V) [46].

Density functional theory (DFT) calculations

The structural changes induced by Zn doping were studied using DFT. Our calculations were performed using the Vienna *ab initio* simulation package (VASP) [47], and the exchange and correlation energy functional was treated by the Perdew-Burke-Ernzerh variant of the generalized gradient approximation (GGA) [48]. Interactions between ions and electrons were described using the projector augmented wave pseudo potentials (PAW) approach, and the energy cutoff for the plane wave basis set was set to 500 eV; the total energy was converged to 10^{-5} eV [49,50]. Effective U parameters of 5.7 and 3.1 eV were used to describe the electronic structures of Co and V, respectively [51]. The lattice parameters of Co_2VO_4 and $\text{CoZn}_{0.5}\text{V}_{1.5}\text{O}_4$ were optimized to be $6.00 \text{ \AA} \times 6.00 \text{ \AA} \times 6.06 \text{ \AA}$ with $\alpha = 120^\circ$, $\beta = 120^\circ$, $\gamma = 89^\circ$ and $6.00 \text{ \AA} \times 6.05 \text{ \AA} \times 6.00 \text{ \AA}$ with $\alpha = \beta = \gamma = 60^\circ$, respectively. Seven k -points were used for k -point sampling in the irreducible region of the first Brillouin zone, which ensured the accuracy of the calculation within 1 meV.

RESULTS AND DISCUSSION

The synthesis process of $\text{CoZn}_{0.5}\text{V}_{1.5}\text{O}_4$ is shown in Fig. S1. Spinel Co_2VO_4 was synthesized by the exchange of 2-MIM^- in Co-MOF by VO_3^- , where one Co occupies the tetrahedral site, and one Co and one V occupy the octahedral sites, as shown in Fig. 1a, b. To replace octahedral cobalt with zinc, a precursor of ZnCo-MOF (Co:Zn = 2:1) was selected for the synthesis of $\text{CoZn}_{0.5}\text{V}_{1.5}\text{O}_4$ (Fig. 1d), and the Co octahedrons were occupied by Zn and V.

The crystalline structures of the materials were investigated using XRD. From the XRD spectra (Fig. 2a), the patterns of $\text{CoZn}_{0.5}\text{V}_{1.5}\text{O}_4$ and Co_2VO_4 are consistent with the standard pattern of Co_2VO_4 (PDF card No. 73-1633) without any peaks corresponding to ZnCo-MOF or Co-MOF (Fig. S2) [52,53], suggesting the formation of $\text{CoZn}_{0.5}\text{V}_{1.5}\text{O}_4$ and Co_2VO_4 , respectively.

In the Raman spectra of $\text{CoZn}_{0.5}\text{V}_{1.5}\text{O}_4$ and Co_2VO_4 (Fig. 2b), the peak at 807 cm^{-1} corresponds to V–O bonds [54], and the peaks at 314 and 477 cm^{-1} are attributed to the tetrahedral Co–O bonds [52,55,56]. Moreover, the peak at 678 cm^{-1} , which is attributed to the octahedral Co–O bonds of Co_2VO_4 , almost disappeared in $\text{CoZn}_{0.5}\text{V}_{1.5}\text{O}_4$, and no peaks corresponding to ZnCo-MOF (Fig. S2) were observed, which suggests that the octahedral Co atoms were replaced by Zn and V atoms [55,56].

XPS was used to examine the surface states of $\text{CoZn}_{0.5}\text{V}_{1.5}\text{O}_4$ and Co_2VO_4 . The full spectra (Fig. 2c) show Co, V, and O elements in both $\text{CoZn}_{0.5}\text{V}_{1.5}\text{O}_4$ and Co_2VO_4 . The extra peak of Zn $2p_{3/2}$ at 1021 eV in $\text{CoZn}_{0.5}\text{V}_{1.5}\text{O}_4$ indicates the presence of Zn. In Co_2VO_4 , the V $2p_{3/2}$ peak (Fig. 2d) corresponds to V^{4+} (516.7 eV). The V $2p_{3/2}$ peak of $\text{CoZn}_{0.5}\text{V}_{1.5}\text{O}_4$ (Fig. 2e) can be deconvoluted into V^{4+} (516.7 eV) and V^{3+} (515.5 eV) [54]. This is because Zn^{2+} reduced V^{4+} to V^{3+} . The O 1s spectrum (Fig. 2f) of $\text{CoZn}_{0.5}\text{V}_{1.5}\text{O}_4$ demonstrates the coexistence of metal–oxygen bonds (529.6 eV), hypoxia defects (531.3 eV), and adsorbed water (531.8 eV) on the surface [41,57].

SEM images (Fig. S3a, c) show that the ZnCo-MOF and Co-MOF nanosheet arrays grow uniformly and are closely arranged on the surface of the NF. From the enlarged views (Fig. S3b, d), the surfaces of the ZnCo-MOF and Co-MOF nanosheets were smooth and similar in size. The nanosheet array structure of $\text{CoZn}_{0.5}\text{V}_{1.5}\text{O}_4$ (Fig. 3a) can still be well maintained after treatment with the NaVO_3 solution. The SEM image of $\text{CoZn}_{0.5}\text{V}_{1.5}\text{O}_4$ (Fig. 3b) reveals that the surface becomes rough, and small particles can be detected. Comparing the $\text{CoZn}_{0.5}\text{V}_{1.5}\text{O}_4$ (Fig. 3c) and Co_2VO_4 nanosheets (Fig. 3d), the thickness of Co_2VO_4 is approximately 250 nm, while that of $\text{CoZn}_{0.5}\text{V}_{1.5}\text{O}_4$ is approximately 180 nm. The nitrogen adsorption/desorption isotherms (Fig. S2c) and BJH pore size distributions (Fig. S2d) show the specific surface area and mesoporous features. The surface areas

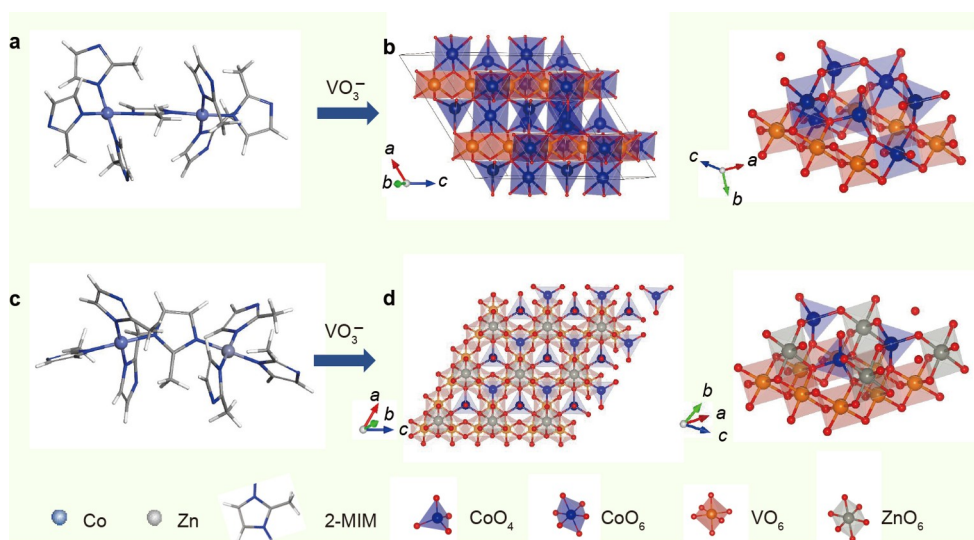


Figure 1 Structures of (a) Co-MOF, (b) Co_2VO_4 , (c) ZnCo-MOF and (d) $\text{CoZn}_{0.5}\text{V}_{1.5}\text{O}_4$.

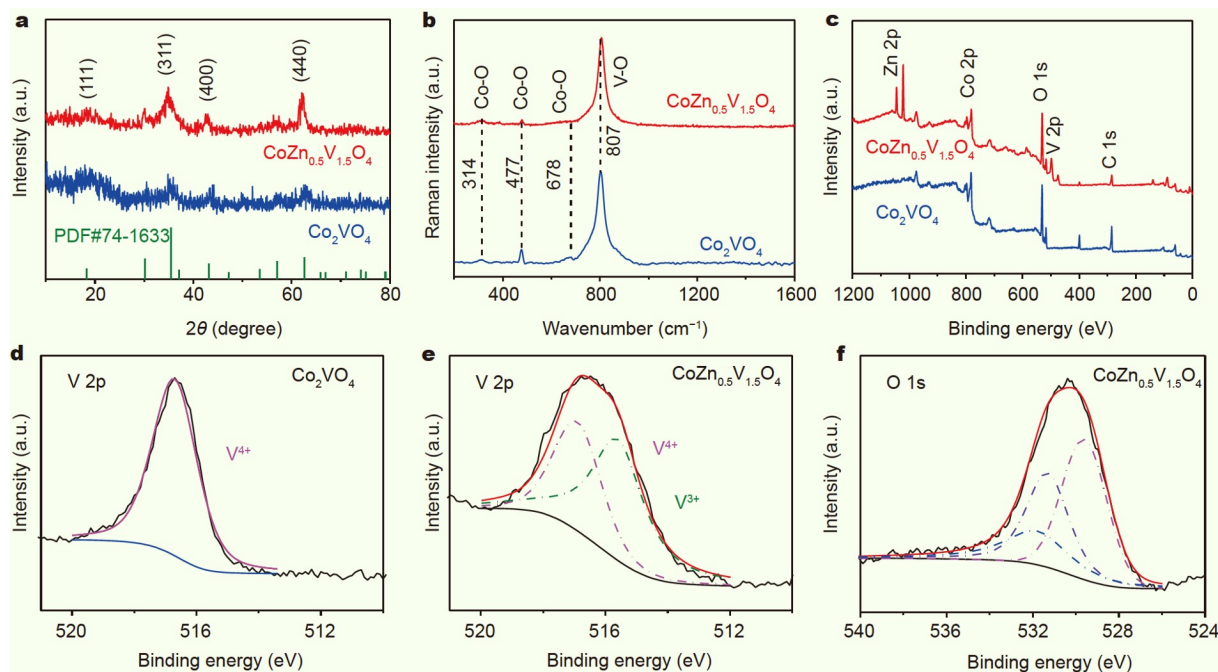


Figure 2 (a) XRD patterns, (b) Raman spectra and (c) XPS full spectra of $\text{CoZn}_{0.5}\text{V}_{1.5}\text{O}_4$ and Co_2VO_4 . (d) V 2p XPS spectra of Co_2VO_4 , (e) V 2p and (f) O 1s XPS spectra of $\text{CoZn}_{0.5}\text{V}_{1.5}\text{O}_4$.

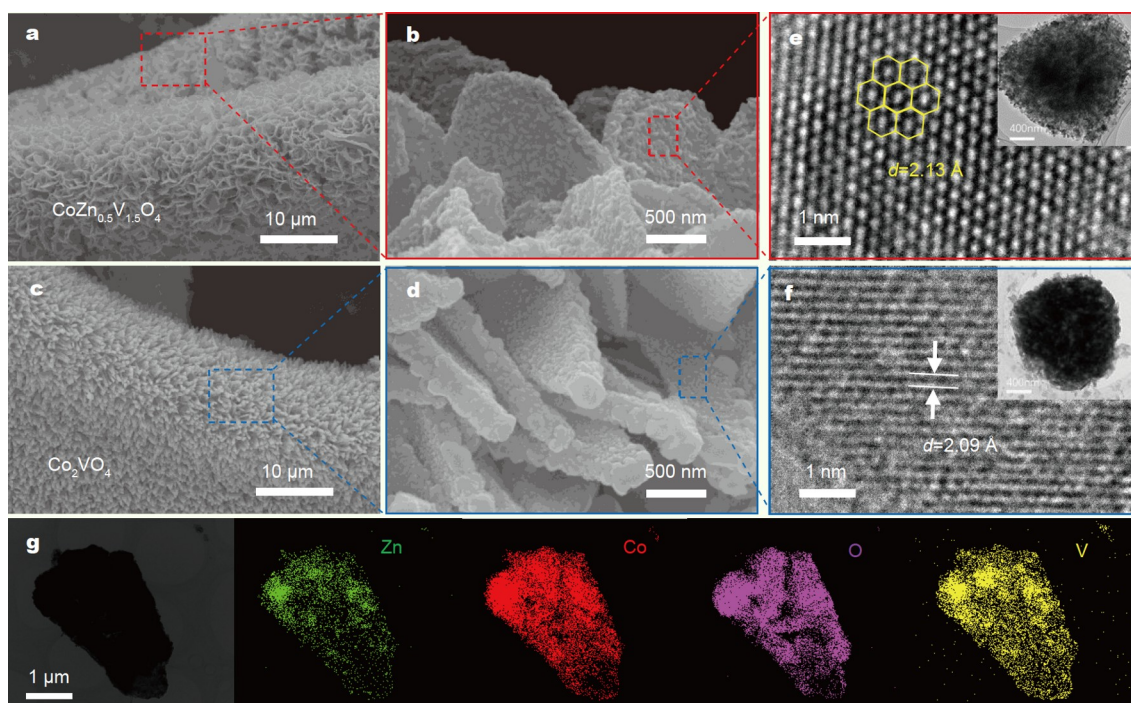


Figure 3 SEM images of (a, b) $\text{CoZn}_{0.5}\text{V}_{1.5}\text{O}_4$ and (c, d) Co_2VO_4 . HRTEM and inserted TEM images of (e) $\text{CoZn}_{0.5}\text{V}_{1.5}\text{O}_4$ and (f) Co_2VO_4 . (g) TEM-EDS element mappings of $\text{CoZn}_{0.5}\text{V}_{1.5}\text{O}_4$.

of the two electrodes were measured using the Brunauer-Emmett-Teller (BET) method. On the NF, the specific surface area of the $\text{CoZn}_{0.5}\text{V}_{1.5}\text{O}_4$ ($11.2 \text{ cm}^2 \text{ g}^{-1}$) is larger than that of Co_2VO_4 ($10.4 \text{ cm}^2 \text{ g}^{-1}$). Thus, doping with Zn does not decrease the specific surface area. The specific surface areas of Co-MOF and ZnCo-MOF are 9.12 and $9.60 \text{ cm}^2 \text{ g}^{-1}$, respectively, as shown in Fig. S4. The specific surface area of ZnCo-MOF was slightly

larger than that of Co-MOF. The specific surface areas of $\text{CoZn}_{0.5}\text{V}_{1.5}\text{O}_4$ and Co_2VO_4 after ion exchange and annealing treatment were improved compared with those of ZnCo-MOF and Co-MOF.

Fig. 3e, f show TEM and HRTEM images of $\text{CoZn}_{0.5}\text{V}_{1.5}\text{O}_4$ and Co_2VO_4 , respectively. The inset TEM images show that the nanosheets are composed of many small dense particles. The

elemental distribution was further confirmed by energy-dispersive X-ray spectrometry (EDS) mapping analysis (Fig. 3g), where Zn, Co, V, and O elements are uniformly distributed on the $\text{CoZn}_{0.5}\text{V}_{1.5}\text{O}_4$ nanosheets. The HRTEM images show obvious lattice fringes of 2.09 Å in the Co_2VO_4 , which matches well with the standard (400) crystal planes of Co_2VO_4 [21]. An expanded d spacing of 2.13 Å is observed in $\text{CoZn}_{0.5}\text{V}_{1.5}\text{O}_4$ for the (400) facets, which is consistent with the XRD results. Further, hexagonal symmetry can be detected, which agrees well with the analyses of Sekhar [20].

DFT calculations were performed to study the changes in the electronic structure of Co_2VO_4 by Zn doping. The structure of Co_2VO_4 is shown in Fig. 1b, where one Co^{2+} cation occupies the tetrahedral site and the other Co^{2+} and V^{4+} occupy the octahedral sites. All the octahedrons of $\text{Co}(\text{O}_6)$ and $\text{V}(\text{O}_6)$ are connected *via* edge-sharing bonds, and the $\text{Co}(\text{O}_4)$ tetrahedrons link with the octahedrons by corner-sharing bonds. Although the surface of Co_2VO_4 is hexagonal, its high Co content makes it exhibit a layered structure [21]. The structure of $\text{CoZn}_{0.5}\text{V}_{1.5}\text{O}_4$ is shown in Fig. 1d, where half of the Co^{2+} octahedrons in Co_2VO_4 are replaced by Zn^{2+} and the other half are replaced by V^{3+} , thus reducing the two V^{4+} ions in Co_2VO_4 to V^{3+} . The new structure exhibited a high hexagonal symmetry.

To understand the electronic properties of Co_2VO_4 and $\text{CoZn}_{0.5}\text{V}_{1.5}\text{O}_4$, DOS analysis was performed, as shown in Fig. 4a, b. Co_2VO_4 behaves as a semiconductor in addition to the existence of V^{4+} , which is similar to VO_2 . This phenomenon has been proposed as a crystalline field splitting of the d orbitals, which is caused by strong electron-electron interactions in metal-metal bonds [58]. Further, projected DOS (PDOS) calculations were used to explain this splitting effect, as shown in

Fig. 4c, d. The 3d electronic levels of the V ion are split into high e_g and low t_{2g} states by hybridization with the O 2p orbitals. The e_g orbitals originate from the anti-bonding V–O bonds (σ -type) above the Fermi level. Because of the edge-sharing of $\text{V}(\text{O}_6)$, the octahedrons are compressed, which separates the t_{2g} orbitals into a single a_{1g} orbital and a doubly generated e'_{g} as π -type V–O bonds [59]. The a_{1g} orbitals are parallel to the c -axis, which affects the metal-metal bonds. When Co^{2+} cations occupy the octahedral sites, high d-d electron correlations between Co–V split the a_{1g} orbitals into a bonding ($\text{V}-a_{1g}$) and anti-bonding combination ($\text{V}-a_{1g}^*$), resulting in an increased p-d overlap (V–O) and an upshift of the π^* -orbitals (V–O) [60]. As shown in Fig. 4c, the $\text{V}-a_{1g}$ orbitals are fully occupied while $\text{V}-a_{1g}^*$ is empty, resulting in a bandgap between the conduction band and valence band. However, when Zn and V replaced the Co^{2+} octahedrons, the d-d electron correlations decreased and one more electron from V^{3+} in the 3d shell existed, resulting in a downshift of the π^* -orbitals (V–O) and half-filled a_{1g} orbitals near the Fermi level, as shown in Fig. 4d. The states near the Fermi level can greatly increase the conductivity of the composite owing to the decrease in metal-metal interaction. A partial charge analysis of the highest occupied molecule orbital (HOMO) band inserted in Fig. 4d also proves the existence of a_{1g} states ($d_{x^2-y^2}$) [60].

The electrochemical performance of $\text{CoZn}_{0.5}\text{V}_{1.5}\text{O}_4$ was measured in a three-electrode system with 2 mol L⁻¹ KOH aqueous solution as the electrolyte. NF-loaded $\text{CoZn}_{0.5}\text{V}_{1.5}\text{O}_4$ was directly applied as the working electrode without extra binder or conductive carbon materials. The Co_2VO_4 was tested under the same conditions for comparison.

The CV curves of $\text{CoZn}_{0.5}\text{V}_{1.5}\text{O}_4$ and Co_2VO_4 at a scanning rate of 5 mV s⁻¹ are shown in Fig. 5a. $\text{CoZn}_{0.5}\text{V}_{1.5}\text{O}_4$ presents a

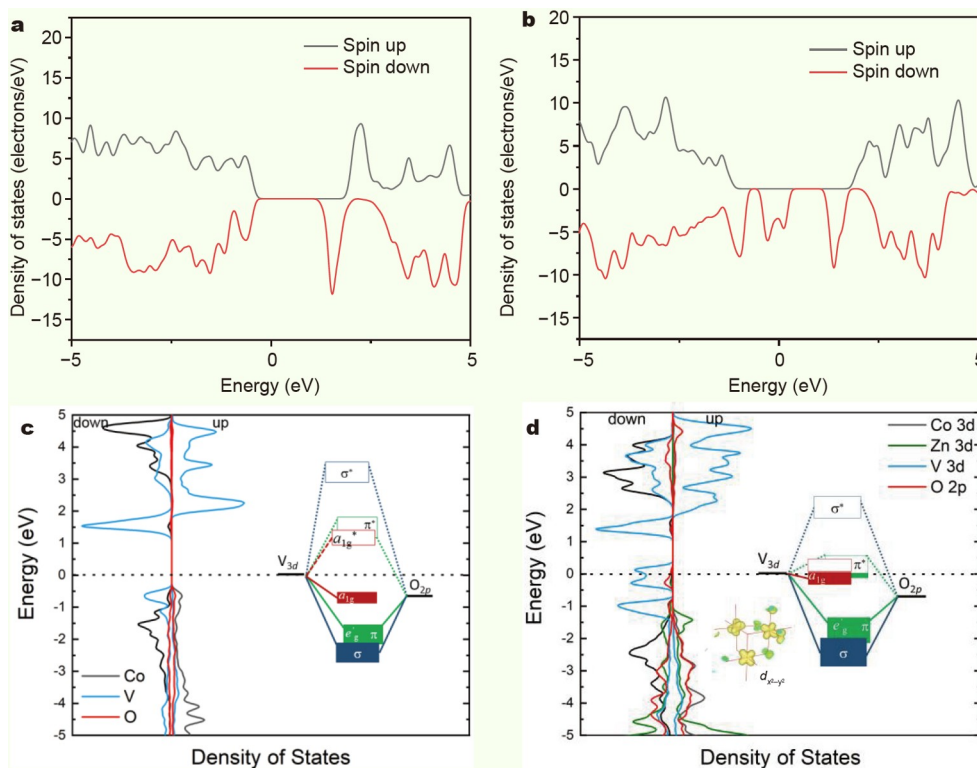


Figure 4 DOSs for (a) Co_2VO_4 and (b) $\text{CoZn}_{0.5}\text{V}_{1.5}\text{O}_4$. PDOSs of (c) Co_2VO_4 and (d) $\text{CoZn}_{0.5}\text{V}_{1.5}\text{O}_4$.

larger CV curve area than Co_2VO_4 , indicating an enhanced specific capacitance for $\text{CoZn}_{0.5}\text{V}_{1.5}\text{O}_4$. The CV curves of $\text{CoZn}_{0.5}\text{V}_{1.5}\text{O}_4$ at different scanning rates are shown in Fig. S5a. A pair of redox peaks belonging to $\text{Co}^{2+}/\text{Co}^{3+}$ [54,61] within the potential range of 0 to 0.45 V in all the CV curves indicates pseudocapacitance energy storage characteristics when used as electrodes for supercapacitors [62]. As the scanning rate increased, the retention rates of the $\text{CoZn}_{0.5}\text{V}_{1.5}\text{O}_4$ CV curves were better than those of Co_2VO_4 , showing a good capacitive output capability at high scanning rates. Fig. S5b shows the GCD curves of $\text{CoZn}_{0.5}\text{V}_{1.5}\text{O}_4$ at different current densities. The curves exhibit nonlinear and approximately symmetric graphical features. They have a pair of charge and discharge level platforms, in agreement with the redox peaks in the CV curves. The GCD curves of $\text{CoZn}_{0.5}\text{V}_{1.5}\text{O}_4$ and Co_2VO_4 at 1 mA cm^{-2} (Fig. 5b) illustrate that $\text{CoZn}_{0.5}\text{V}_{1.5}\text{O}_4$ has a longer discharge time than Co_2VO_4 , indicating that $\text{CoZn}_{0.5}\text{V}_{1.5}\text{O}_4$ has a larger specific capacitance. In addition, the GCD curve of Co_2VO_4 has poor symmetry, and the calculated coulombic efficiency is only 82%,

while that of $\text{CoZn}_{0.5}\text{V}_{1.5}\text{O}_4$ is as high as 99%. As the current density increased, the coulombic efficiency of $\text{CoZn}_{0.5}\text{V}_{1.5}\text{O}_4$ approaches 100%. The capacitance values of $\text{CoZn}_{0.5}\text{V}_{1.5}\text{O}_4$ and Co_2VO_4 (Fig. 5c) can be calculated using the GCD curve. The capacitances of $\text{CoZn}_{0.5}\text{V}_{1.5}\text{O}_4$ are 1100, 1050, 966, 949, and 890 mF cm^{-2} at current densities of 1, 3, 5, 7, and 10 mA cm^{-2} , respectively, which are higher than those of Co_2VO_4 (915, 880, 845, 710, 599 mF cm^{-2}). When the current density was increased from 1 to 10 mA cm^{-2} , the capacitance of $\text{CoZn}_{0.5}\text{V}_{1.5}\text{O}_4$ was 81%. Co_2VO_4 delivered a capacitance of 915 mF cm^{-2} at 1 mA cm^{-2} , and only 65% remained when the current density was increased to 10 mA cm^{-2} . In Fig. 5d, when the power density is 0.225 mW cm^{-2} , the energy density of $\text{CoZn}_{0.5}\text{V}_{1.5}\text{O}_4$ is $0.031 \text{ mW h cm}^{-2}$, which is higher than that of Co_2VO_4 ($0.026 \text{ mW h cm}^{-2}$) and other reported multi-metal compounds [20,52,63]. The above studies show that replacement with zinc can effectively improve the coulombic efficiency, capacitance content, and rate performance of Co_2VO_4 .

The peak current (i) and scanning rate (v) satisfy the rela-

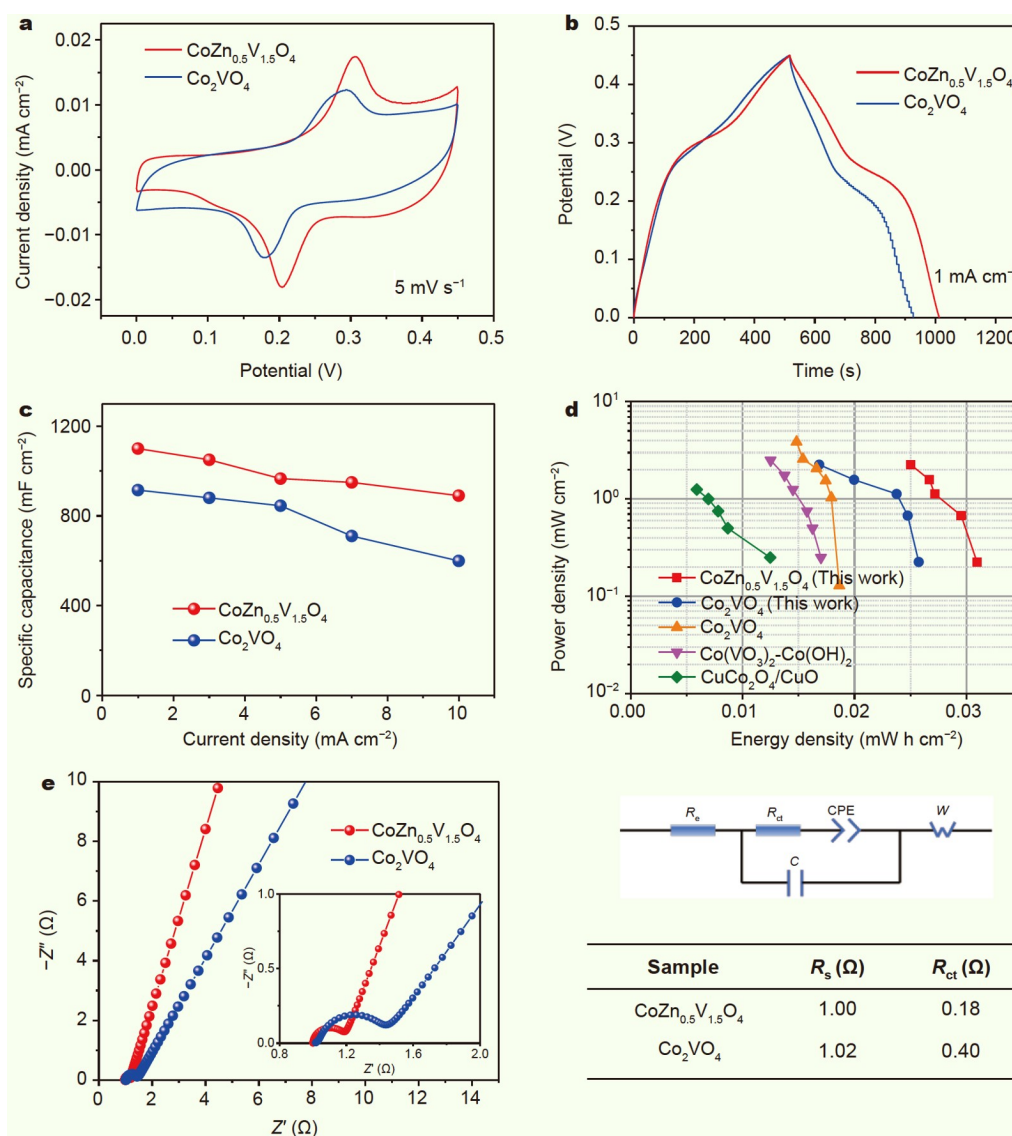


Figure 5 Comparison of (a) CV curves at 5 mV s^{-1} , (b) GCD curves at 1 mA cm^{-2} , (c) specific capacitances, (d) Ragone plots, (e) Nyquist plots and the fitting results based on $\text{CoZn}_{0.5}\text{V}_{1.5}\text{O}_4$ and Co_2VO_4 electrodes.

Table 1 Comparison of capacitance, energy density, and cycle stabilities of some similar materials reported and the present work

Electrode materials	Capacitance (mF cm ⁻²)	Energy density (mW h cm ⁻²)	Cycle stability (%)	Ref.
CoZn _{0.5} V _{1.5} O ₄	1100 (1 mA cm ⁻²)	0.031 (0.225 mW cm ⁻²)	99.4 (10 mA cm ⁻² , 18,000 cycles)	This work
Co ₂ VO ₄	915 (1 mA cm ⁻²)	0.026 (0.225 mW cm ⁻²)	87 (10 mA cm ⁻² , 18,000 cycles)	
rGO@Co ₂ VO ₄	806.4 (1 mA cm ⁻²)	0.028 (0.25 mW cm ⁻²)	101.7 (10 mA cm ⁻² , 4000 cycles)	[20]
Co ₂ VO ₄	481 (1 mA cm ⁻²)	0.018 (0.25 mW cm ⁻²)	-	
Co(VO ₃) ₂ ·Co(OH) ₂	522 (0.5 mA cm ⁻²)	0.018 (0.125 mW cm ⁻²)	90 (10 mA cm ⁻² , 15,000 cycles)	[52]
CuCo ₂ O ₄ /CuO	359 (1 mA cm ⁻²)	0.0125 (0.25 mW cm ⁻²)	79 (5 mA cm ⁻² , 5000 cycles)	[63]

tionship $I = av^b$, where b can be calculated by fitting the linear relations of $\log i$ and $\log v$ [64]. When $b = 0.5$, the electrode process corresponds to diffusion control. When $b = 1$, the electrode exhibits ideal capacitive behavior. The b value of CoZn_{0.5}V_{1.5}O₄ and Co₂VO₄ are 0.7 (Fig. 6a) and 0.68 (Fig. S6), which indicates that the material exhibits both diffusion control and capacitance control behaviors. Meanwhile, the current at a particular sweep rate can be divided into capacitive contribution current and diffusion contribution current, expressed as $i(V) = k_1v + k_2v^{1/2}$, where k_1v and $k_2v^{1/2}$ present the capacitive contribution current and diffusion contribution current, respectively [65]. The formula was used to calculate the capacitance and diffusion contributions in CoZn_{0.5}V_{1.5}O₄ at a CV current of 5 mV s⁻¹, and the corresponding results are shown in Fig. 6b. The capacitance control process of the surface adsorption process accounts for 63%; thus, the material exhibits rapid and reversible charging behavior. With an increase in the scanning rate, the diffusion contribution decreases, and capacitance control gradually dominates. This is because of the insufficient redox reaction of active substances in the electrode materials at high sweep speeds (Figs S7 and S8b). The oxidation reaction of K_xCo₂VO₄ is a competitive reaction between the electrode and electrolyte. In the low voltage range of the oxidation process, the electron energy level, which originates from the K ion absorption during the reduction process, is higher than that of the electrolyte; thus, the K ions return to the electrolyte, which is called the surface capacity. When the oxidation voltage is higher, the energy level of the unoccupied orbital is lower than that of the electrolyte, and the reaction between KOH and Co₂VO₄ occurs. These phenomena can be explained by the capacitive contribution analysis in Fig. 6b and Fig. S8a, where blue represents the surface capacitive contribution. As shown in Fig. S8a, the surface reaction of Co₂VO₄ has been fully reacted

before 0.4 V. Further, between 0.4 and 0.45 V, an irreversible side reaction between electrode material and electrolyte occurs and causes asymmetrical charge-discharge curve. However, for CoZn_{0.5}V_{1.5}O₄ in Fig. 6b, a small oxidation peak exists in the high voltage range of 0.4–0.45 V, which indicates that the surface reaction of CoZn_{0.5}V_{1.5}O₄ is stronger than that between CoZn_{0.5}V_{1.5}O₄ and KOH in the high voltage range, thus resulting in a high coulomb efficiency and symmetrical charge-discharge curves.

The kinetic factors for the enhanced electrochemical performance were analyzed using alternating current (AC) impedance spectroscopy. EIS curves (Fig. 5e) consist of steep straight lines in the low-frequency region (related to charge diffusion) and semicircles in the high-frequency region (related to charge transfer) [46]. From the EIS, the electrolyte resistances (R_e) of CoZn_{0.5}V_{1.5}O₄ and Co₂VO₄ are similar. The electron transfer resistance (R_{ct}) of CoZn_{0.5}V_{1.5}O₄ (0.18 Ω) is smaller than that of Co₂VO₄ (0.4 Ω), indicating fast electron transfer ability. Meanwhile, the slope of CoZn_{0.5}V_{1.5}O₄ in the low-frequency region is larger than that of Co₂VO₄; thus, its ion diffusion kinetics is enhanced by the addition of Zn [66]. Hence, the doping of Zn in CoZn_{0.5}V_{1.5}O₄ increases the electron transfer and ion diffusion speed, which is in good agreement with the calculation results.

The cycling performances of the CoZn_{0.5}V_{1.5}O₄ and Co₂VO₄ electrodes were tested at a current density of 10 mA cm⁻². As shown in Fig. 7a, the specific capacitance of the CoZn_{0.5}V_{1.5}O₄ electrode retained 99.4% of its initial capacitance after 18,000 charge/discharge cycles, and the retention of the Co₂VO₄ electrode was only 87%, indicating improved cycling durability of CoZn_{0.5}V_{1.5}O₄. In the SEM after 18,000 cycles (Fig. 7e), the structure of Co₂VO₄ changed from nanosheets to nanoparticles owing to the large resistance of charge diffusion during the electrochemical reaction. The morphology of the CoZn_{0.5}V_{1.5}O₄

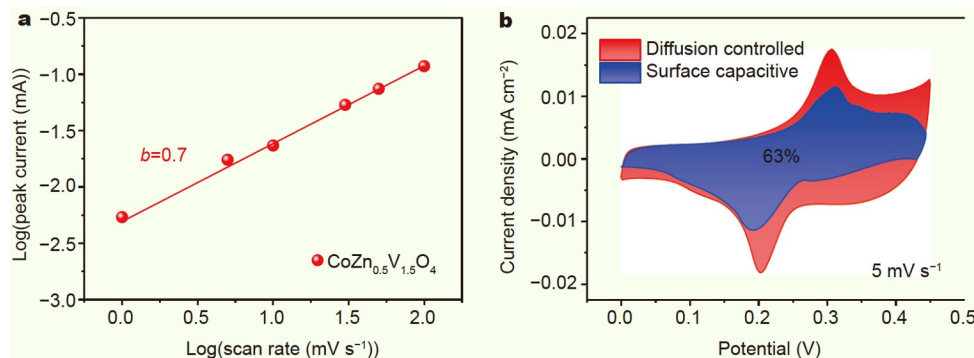


Figure 6 (a) Determination of the b -value using the relationship between the peak current and scan rate of CoZn_{0.5}V_{1.5}O₄ electrode. (b) Capacitive contribution to the total current from CV analysis at 5 mV s⁻¹ of CoZn_{0.5}V_{1.5}O₄ electrode.

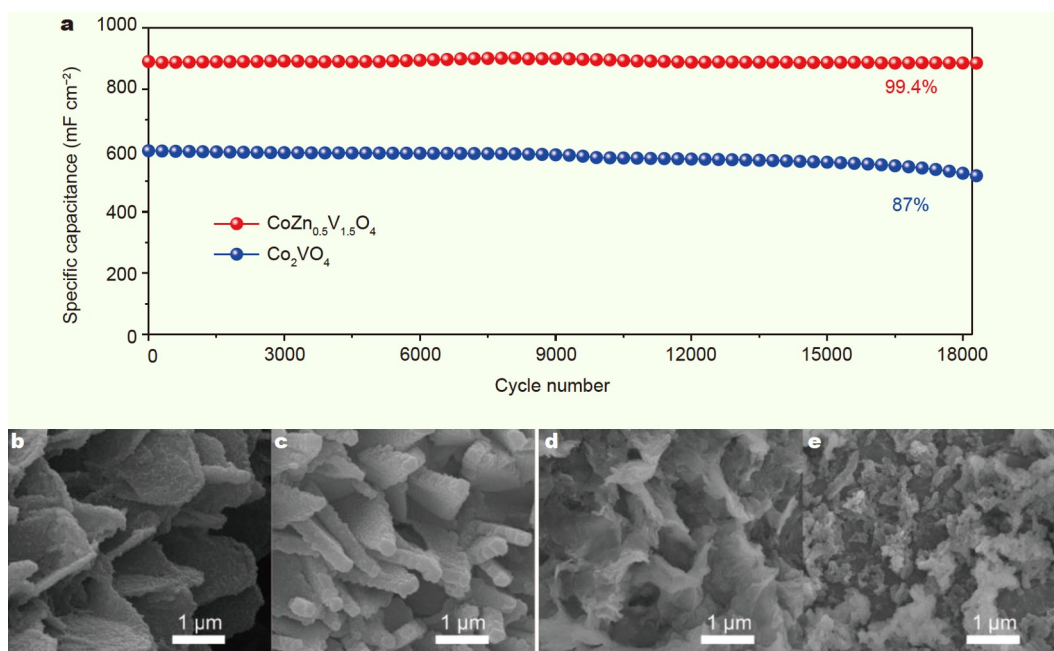


Figure 7 (a) Cycling performances of $\text{CoZn}_{0.5}\text{V}_{1.5}\text{O}_4$ and Co_2VO_4 electrodes at 10 mA cm^{-2} . SEM images of (b) $\text{CoZn}_{0.5}\text{V}_{1.5}\text{O}_4$ and (c) Co_2VO_4 electrodes. SEM images of (d) cycled $\text{CoZn}_{0.5}\text{V}_{1.5}\text{O}_4$ and (e) cycled Co_2VO_4 electrodes after 18,000 cycles.

nanosheets (Fig. 7d) is retained, indicating that the introduction of Zn ions can improve the structural stability of the Zn–O covalent bond.

CONCLUSION

Spinel-structured $\text{CoZn}_{0.5}\text{V}_{1.5}\text{O}_4$ was fabricated by ion exchange annealing treatment, and the electronic structures of Co_2VO_4 and $\text{CoZn}_{0.5}\text{V}_{1.5}\text{O}_4$ were studied by DFT calculations. In $\text{CoZn}_{0.5}\text{V}_{1.5}\text{O}_4$, the replacement of Co octahedrons by Zn causes the π^* -orbitals (V–O) and half-filled a_{1g} orbitals to downshift near Fermi level, which significantly increases the conductivity of $\text{CoZn}_{0.5}\text{V}_{1.5}\text{O}_4$. Meanwhile, Zn preferentially forms a covalent bond, which improves lattice stability and cycle durability. The capacitance of $\text{CoZn}_{0.5}\text{V}_{1.5}\text{O}_4$ was 1100 mF cm^{-2} at 1 mA cm^{-2} , and remained at 81% when the current density increased by 10 times. $\text{CoZn}_{0.5}\text{V}_{1.5}\text{O}_4$ also shows excellent cycling durability, retaining 99.4% of its initial capacitance after 18,000 charge/discharge cycles. This work offers the possibility of designing octahedral and tetrahedral sites in spinel structures to suppress metal-metal interactions, which provides some guidance for the modulation of the crystal field of transition metals in catalysis, solar energy, and other energy storage devices.

Received 14 April 2021; accepted 27 May 2021;
published online 20 July 2021

- Fang G, Zhou J, Pan A, *et al.* Recent advances in aqueous zinc-ion batteries. *ACS Energy Lett*, 2018, 3: 2480–2501
- Yu L, Yu XY, Lou XWD. The design and synthesis of hollow micro-/nanostructures: Present and future trends. *Adv Mater*, 2018, 30: 1800939
- Chu S, Majumdar A. Opportunities and challenges for a sustainable energy future. *Nature*, 2012, 488: 294–303
- Mai LQ, Minhas-Khan A, Tian X, *et al.* Synergistic interaction between redox-active electrolyte and binder-free functionalized carbon for ultrahigh supercapacitor performance. *Nat Commun*, 2013, 4: 2923

- Zhu G, Yang L, Wang W, *et al.* Hierarchical three-dimensional manganese doped cobalt phosphide nanowire decorated nanosheet cluster arrays for high-performance electrochemical pseudocapacitor electrodes. *Chem Commun*, 2018, 54: 9234–9237
- Qin T, Liu B, Wen Y, *et al.* Freestanding flexible graphene foams @polypyrrole/MnO₂ electrodes for high-performance supercapacitors. *J Mater Chem A*, 2016, 4: 9196–9203
- Yang T, Liang J, Sultana I, *et al.* Formation of hollow MoS₂/carbon microspheres for high capacity and high rate reversible alkali-ion storage. *J Mater Chem A*, 2018, 6: 8280–8288
- Liu Q, Shi H, Yang T, *et al.* Sequential growth of hierarchical N-doped carbon-MoS₂ nanocomposites with variable nanostructures. *J Mater Chem A*, 2019, 7: 6197–6204
- Wang G, Zhang L, Zhang J. A review of electrode materials for electrochemical supercapacitors. *Chem Soc Rev*, 2012, 41: 797–828
- Sahu V, Shekhar S, Sharma RK, *et al.* Ultrahigh performance supercapacitor from lacey reduced graphene oxide nanoribbons. *ACS Appl Mater Interfaces*, 2015, 7: 3110–3116
- Ma Q, Yu Y, Sindoro M, *et al.* Carbon-based functional materials derived from waste for water remediation and energy storage. *Adv Mater*, 2017, 29: 1605361
- Gao M, Wang WK, Rong Q, *et al.* Porous ZnO-coated Co₃O₄ nanorod as a high-energy-density supercapacitor material. *ACS Appl Mater Interfaces*, 2018, 10: 23163–23173
- Wang F, Wu X, Yuan X, *et al.* Latest advances in supercapacitors: From new electrode materials to novel device designs. *Chem Soc Rev*, 2017, 46: 6816–6854
- Jiang L, Yuan X, Liang J, *et al.* Nanostructured core-shell electrode materials for electrochemical capacitors. *J Power Sources*, 2016, 331: 408–425
- Liu T, Finn L, Yu M, *et al.* Polyaniline and polypyrrole pseudocapacitor electrodes with excellent cycling stability. *Nano Lett*, 2014, 14: 2522–2527
- Kim J, Young C, Lee J, *et al.* Nanoarchitecture of MOF-derived nanoporous functional composites for hybrid supercapacitors. *J Mater Chem A*, 2017, 5: 15065–15072
- Han SA, Lee J, Shim K, *et al.* Strategically designed zeolitic imidazolate frameworks for controlling the degree of graphitization. *Bull Chem Soc Jpn*, 2018, 91: 1474–1480

- 18 Qutaish H, Lee J, Hyeon Y, *et al.* Design of cobalt catalysed carbon nanotubes in bimetallic zeolitic imidazolate frameworks. *Appl Surf Sci*, 2021, 547: 149134
- 19 Lee J, Choi SH, Qutaish H, *et al.* Structurally stabilized lithium-metal anode *via* surface chemistry engineering. *Energy Storage Mater*, 2021, 37: 315–324
- 20 Chandra Sekhar S, Nagaraju G, Narsimulu D, *et al.* Graphene matrix sheathed metal vanadate porous nanospheres for enhanced longevity and high-rate energy storage devices. *ACS Appl Mater Interfaces*, 2020, 12: 27074–27086
- 21 Mu C, Mao J, Guo J, *et al.* Rational design of spinel cobalt vanadate oxide Co_2VO_4 for superior electrocatalysis. *Adv Mater*, 2020, 32: 1907168
- 22 Abe H, Liu J, Ariga K. Catalytic nanoarchitectonics for environmentally compatible energy generation. *Mater Today*, 2016, 19: 12–18
- 23 Chen C, Kang Y, Huo Z, *et al.* Highly crystalline multimetallic nano-frames with three-dimensional electrocatalytic surfaces. *Science*, 2014, 343: 1339–1343
- 24 Liu H, Zhu Z, Yan Q, *et al.* A disordered rock salt anode for fast-charging lithium-ion batteries. *Nature*, 2020, 585: 63–67
- 25 Ling T, Da P, Zheng X, *et al.* Atomic-level structure engineering of metal oxides for high-rate oxygen intercalation pseudocapacitance. *Sci Adv*, 2018, 4: eaau6261
- 26 Yang J, Zheng C, Xiong P, *et al.* Zn-doped Ni-MOF material with a high supercapacitive performance. *J Mater Chem A*, 2014, 2: 19005–19010
- 27 Niu J, Shao R, Liang J, *et al.* Biomass-derived mesopore-dominant porous carbons with large specific surface area and high defect density as high performance electrode materials for Li-ion batteries and supercapacitors. *Nano Energy*, 2017, 36: 322–330
- 28 Sheberla D, Bachman JC, Elias JS, *et al.* Conductive MOF electrodes for stable supercapacitors with high areal capacitance. *Nat Mater*, 2017, 16: 220–224
- 29 Xiao Z, Mei Y, Yuan S, *et al.* Controlled hydrolysis of metal-organic frameworks: Hierarchical Ni/Co-layered double hydroxide microspheres for high-performance supercapacitors. *ACS Nano*, 2019, 13: 7024–7030
- 30 Salunkhe RR, Kaneti YV, Yamauchi Y. Metal-organic framework-derived nanoporous metal oxides toward supercapacitor applications: Progress and prospects. *ACS Nano*, 2017, 11: 5293–5308
- 31 Guan BY, Yu XY, Wu HB, *et al.* Complex nanostructures from materials based on metal-organic frameworks for electrochemical energy storage and conversion. *Adv Mater*, 2017, 29: 1703614
- 32 Wang C, Kaneti YV, Bando Y, *et al.* Metal-organic framework-derived one-dimensional porous or hollow carbon-based nanofibers for energy storage and conversion. *Mater Horiz*, 2018, 5: 394–407
- 33 Zhang H, Liu X, Wu Y, *et al.* MOF-derived nanohybrids for electrocatalysis and energy storage: Current status and perspectives. *Chem Commun*, 2018, 54: 5268–5288
- 34 Indra A, Song T, Paik U. Metal organic framework derived materials: Progress and prospects for the energy conversion and storage. *Adv Mater*, 2018, 30: 1705146
- 35 Gumilar G, Kaneti YV, Henzie J, *et al.* General synthesis of hierarchical sheet/plate-like M-BDC (M = Cu, Mn, Ni, and Zr) metal-organic frameworks for electrochemical non-enzymatic glucose sensing. *Chem Sci*, 2020, 11: 3644–3655
- 36 Bai Y, Zhang G, Zheng S, *et al.* Pyridine-modulated Ni/Co bimetallic metal-organic framework nanoplates for electrocatalytic oxygen evolution. *Sci China Mater*, 2021, 64: 137–148
- 37 Li D, Xu HQ, Jiao L, *et al.* Metal-organic frameworks for catalysis: State of the art, challenges, and opportunities. *EnergyChem*, 2019, 1: 100005
- 38 Li Q, Li X, Gu J, *et al.* Porous rod-like $\text{Ni}_2\text{P}/\text{Ni}$ assemblies for enhanced urea electrooxidation. *Nano Res*, 2021, 14: 1405–1412
- 39 Salunkhe RR, Tang J, Kobayashi N, *et al.* Ultrahigh performance supercapacitors utilizing core-shell nanoarchitectures from a metal-organic framework-derived nanoporous carbon and a conducting polymer. *Chem Sci*, 2016, 7: 5704–5713
- 40 Zhang S, Xia W, Yang Q, *et al.* Core-shell motif construction: Highly graphitic nitrogen-doped porous carbon electrocatalysts using MOF-derived carbon@COF heterostructures as sacrificial templates. *Chem Eng J*, 2020, 396: 125154
- 41 Guan C, Liu X, Ren W, *et al.* Rational design of metal-organic framework derived hollow NiCo_2O_4 arrays for flexible supercapacitor and electrocatalysis. *Adv Energy Mater*, 2017, 7: 1602391
- 42 Young C, Kim J, Kaneti YV, *et al.* One-step synthetic strategy of hybrid materials from bimetallic metal-organic frameworks for supercapacitor applications. *ACS Appl Energy Mater*, 2018, 1: 2007–2015
- 43 Guan BY, Yu L, Wang X, *et al.* Formation of onion-like NiCo_2S_4 particles *via* sequential ion-exchange for hybrid supercapacitors. *Adv Mater*, 2017, 29: 1605051
- 44 Yang Y, Li ML, Lin JN, *et al.* MOF-derived Ni_3S_4 encapsulated in 3D conductive network for high-performance supercapacitor. *Inorg Chem*, 2020, 59: 2406–2412
- 45 Zhang S, Li D, Chen S, *et al.* Highly stable supercapacitors with MOF-derived Co_9S_8 /carbon electrodes for high rate electrochemical energy storage. *J Mater Chem A*, 2017, 5: 12453–12461
- 46 Bi W, Jahrman E, Seidler G, *et al.* Tailoring energy and power density through controlling the concentration of oxygen vacancies in V_2O_5 /PEDOT nanocable-based supercapacitors. *ACS Appl Mater Interfaces*, 2019, 11: 16647–16655
- 47 Kresse G, Furthmüller J. Efficiency of *ab-initio* total energy calculations for metals and semiconductors using a plane-wave basis set. *Comput Mater Sci*, 1996, 6: 15–50
- 48 Perdew JP, Burke K, Ernzerhof M. Generalized gradient approximation made simple. *Phys Rev Lett*, 1996, 77: 3865–3868
- 49 Blöchl PE. Projector augmented-wave method. *Phys Rev B*, 1994, 50: 17953–17979
- 50 Kresse G, Joubert D. From ultrasoft pseudopotentials to the projector augmented-wave method. *Phys Rev B*, 1999, 59: 1758–1775
- 51 Mueller T, Hautier G, Jain A, *et al.* Evaluation of favorite-structured cathode materials for lithium-ion batteries using high-throughput computing. *Chem Mater*, 2011, 23: 3854–3862
- 52 Zhang Y, Chen H, Guan C, *et al.* Energy-saving synthesis of MOF-derived hierarchical and hollow $\text{Co}(\text{VO}_3)_2\text{-Co}(\text{OH})_2$ composite leaf arrays for supercapacitor electrode materials. *ACS Appl Mater Interfaces*, 2018, 10: 18440–18444
- 53 Kong D, Wang Y, Huang S, *et al.* 3D self-branched zinc-cobalt oxide@N-doped carbon hollow nanowall arrays for high-performance asymmetric supercapacitors and oxygen electrocatalysis. *Energy Storage Mater*, 2019, 23: 653–663
- 54 Wang Y, Chai H, Dong H, *et al.* Superior cycle stability performance of quasi-cuboidal CoV_2O_6 microstructures as electrode material for supercapacitors. *ACS Appl Mater Interfaces*, 2016, 8: 27291–27297
- 55 Fan X, Guan J, Cao X, *et al.* Low-temperature synthesis, magnetic and microwave electromagnetic properties of substoichiometric spinel cobalt ferrite octahedra. *Eur J Inorg Chem*, 2010, 2010(3): 419–426
- 56 Wang X, Liu Y, Zhang T, *et al.* Geometrical-site-dependent catalytic activity of ordered mesoporous Co-based spinel for benzene oxidation: *In situ* DRIFTS study coupled with Raman and XAFS spectroscopy. *ACS Catal*, 2017, 7: 1626–1636
- 57 Guan C, Wang Y, Hu Y, *et al.* Conformally deposited NiO on a hierarchical carbon support for high-power and durable asymmetric supercapacitors. *J Mater Chem A*, 2015, 3: 23283–23288
- 58 Goodenough JB. The two components of the crystallographic transition in VO_2 . *J Solid State Chem*, 1971, 3: 490–500
- 59 Landron S, Lepetit MB. Importance of $t_{2g}\text{-}e_g$ hybridization in transition metal oxides. *Phys Rev B*, 2008, 77: 125106
- 60 Aetukuri NB, Gray AX, Drouard M, *et al.* Control of the metal-insulator transition in vanadium dioxide by modifying orbital occupancy. *Nat Phys*, 2013, 9: 661–666
- 61 Liu S, Sarwar S, Zhang H, *et al.* One-step microwave-controlled synthesis of $\text{CoV}_2\text{O}_6\cdot 2\text{H}_2\text{O}$ nanosheet for super long cycle-life battery-type supercapacitor. *Electrochim Acta*, 2020, 364: 137320
- 62 Sun W, Du Y, Wu G, *et al.* Constructing metallic zinc-cobalt sulfide hierarchical core-shell nanosheet arrays derived from 2D metal-organic-frameworks for flexible asymmetric supercapacitors with ul-

- trahigh specific capacitance and performance. *J Mater Chem A*, 2019, 7: 7138–7150
- 63 Shanmugavani A, Selvan RK. Improved electrochemical performances of $\text{CuCo}_2\text{O}_4/\text{CuO}$ nanocomposites for asymmetric supercapacitors. *Electrochim Acta*, 2016, 188: 852–862
- 64 Li H, Lang J, Lei S, *et al.* A high-performance sodium-ion hybrid capacitor constructed by metal-organic framework-derived anode and cathode materials. *Adv Funct Mater*, 2018, 28: 1800757
- 65 Augustyn V, Come J, Lowe MA, *et al.* High-rate electrochemical energy storage through Li^+ intercalation pseudocapacitance. *Nat Mater*, 2013, 12: 518–522
- 66 Bi W, Wang J, Jahrman EP, *et al.* Interface engineering V_2O_5 nanofibers for high-energy and durable supercapacitors. *Small*, 2019, 15: 1901747

Acknowledgements This work was supported by the National Natural Science Foundation of China (51872204, 52072261 and 22011540379), the National Key Research and Development Program of China (2017YFA0204600), Shanghai Social Development Science and Technology Project (20dz1201800), and Shanghai Sailing Program (21YF1430900).

Author contributions Yuan F and Gao G designed the experiments; Yuan F performed the experiments and wrote the original draft; Gao G contributed to the theoretical analysis; Yuan F, Jiang X, Su Y, Guo J and Bao Z performed the data analysis; Gao G, Bi W, Shen J, Bao Z and Wu G supervised the study; Gao G, Bi W and Wu G developed the concept and revised the manuscript. All authors contributed to the general discussion.

Conflict of interest The authors declare that they have no conflict of interest.

Supplementary information Supporting data are available in the online version of the paper.



Fang Yuan is now a master's degree candidate at the School of Physical Science and Engineering, Tongji University. Her research interest focuses on metal-organic frameworks, energy storage and supercapacitors.



Guohua Gao is an associate professor at the School of Physical Science and Engineering, Tongji University. He obtained his PhD degree in materials physics and chemistry from Tongji University in 2010. His main research interests focus on energy storage and conversion, first principles, and vanadium-based nano-hybrids.



Wenchao Bi received her PhD degree in physics from Tongji University in 2020. She was a joint PhD candidate of the University of Washington (Seattle) in 2017–2019. She joined the Departments of Physics, College of Science, University of Shanghai for Science and Technology in 2020. Her research focuses on electrode material design and energy storage mechanism exploration of batteries and supercapacitors.



Guangming Wu is a professor at the School of Physical Science and Engineering, Tongji University. He obtained his PhD degree in condensed matter physics from Tongji University in 1998. His main research interests focus on functional nanomaterials, artificial regulation of micronano structure, energy storage and energy saving.

用于超级电容器的二维金属有机框架衍生的 $\text{CoZn}_{0.5}\text{V}_{1.5}\text{O}_4$ 抑制金属-金属相互作用研究

袁方¹, 高国华^{1*}, 姜小迪¹, 毕文超^{2*}, 苏怡璇¹, 郭靖雯², 包志豪¹, 沈军¹, 吴广明^{1*}

摘要 具有四面体钴和八面体钴的 Co_2VO_4 在电催化和电池领域已取得重要进展。然而，金属-金属之间强的相互作用会降低活性物质的电导率，又会影响表面反应活性，因此同时提升超级电容器活性、电导率和稳定性具有挑战性。本工作利用锌-钴金属有机骨架(ZnCo-MOF)的离子交换合成了具有高比表面的尖晶石结构 $\text{CoZn}_{0.5}\text{V}_{1.5}\text{O}_4$ 。密度泛函理论计算表明，用锌取代过渡金属可以减少过渡金属之间的相互作用，使 π^* 轨道(V-O)和半满的 a_{1g} 轨道下移至费米能级附近，从而提高 $\text{CoZn}_{0.5}\text{V}_{1.5}\text{O}_4$ 的电导率和稳定性。作为超级电容器电极， $\text{CoZn}_{0.5}\text{V}_{1.5}\text{O}_4$ 具有较高的循环稳定性(18,000次循环后电容保持率为99.4%)和比容量(1 mA cm^{-2} 时为 1100 mF cm^{-2})。这项工作为设计过渡金属八面体和四面体的位置以提高材料的电化学性能提供了可能性。